

The Rossiter – McLaughlin effect and analytic radial velocity curves for transiting extrasolar planetary systems

Yasuhiro Ohta, Atsushi Taruya¹ and Yasushi Suto¹

Department of Physics, The University of Tokyo, Tokyo 113-0033, Japan

`ohta@utap.phys.s.u-tokyo.ac.jp, ataruya@utap.phys.s.u-tokyo.ac.jp,`
`suto@phys.s.u-tokyo.ac.jp`

ABSTRACT

A transiting extrasolar planet sequentially blocks off the light coming from the different parts of the disk of the host star in a time dependent manner. Due to the spin of the star, this produces an asymmetric distortion in the line profiles of the stellar spectrum, leading to an apparent anomaly of the radial velocity curves, known as the Rossiter – McLaughlin effect. Here, we derive approximate but accurate analytic formulae for the anomaly of radial velocity curves taking account of the stellar limb darkening. The formulae are particularly useful in extracting information of the projected angle between the planetary orbit axis and the stellar spin axis, λ , and the projected stellar spin velocity, $V \sin I_s$. We create mock samples for the radial curves for the transiting extrasolar system HD209458, and demonstrate that constraints on the spin parameters ($V \sin I_s$, λ) may be significantly improved by combining our analytic template formulae and the precision velocity curves from high-resolution spectroscopic observations with 8–10 m class telescopes. Thus future observational exploration of transiting systems using the Rossiter – McLaughlin effect is one of the most important probes to better understanding of the origin of extrasolar planetary systems, especially the origin of their angular momentum.

Subject headings: planets and satellites: individual (HD209458b), techniques: spectroscopic

¹also at Research Center for the Early Universe(RESCEU), School of Science, The University of Tokyo, Tokyo 113-0033, Japan.

1. Introduction

With more than 130 extrasolar planets discovered so far, major scientific purposes in this field are rapidly moving from mere detection to characterization of the planetary systems, i.e., statistics of planetary masses, orbital periods, eccentricities, stellar metallicities and so on. Most of them have been discovered through the periodic change of radial velocities of central stars. One of them, HD209458b, was first discovered spectroscopically and soon later found to exhibit a transit signature in front of the stellar disk for a duration of ~ 2 hr in its orbital period of 3.5 day (Henry et al. 2000; Charbonneau et al. 2000). More recently a few additional extrasolar planets have been discovered, first photometrically from their transiting signature in their light-curves, and then later confirmed spectroscopically (e.g., Bouchy et al. 2004; Alonso et al. 2004).

Indeed such transiting planets provide important information for the extrasolar planetary systems otherwise unavailable; planetary size, atmospheric composition and the degree of the (mis)alignment of the planetary orbit axis and the stellar spin axis. Among others Queloz et al. (2000) showed that the planetary orbit and the stellar rotation of the HD209458 system share the same direction; the planet sequentially blocks off the light from the approaching and then from the receding parts of the stellar surface. This produces a distortion in the line profiles of the stellar spectrum during the transit in a time-dependent manner, leading to an anomaly of the radial velocity curves, previously known as the Rossiter – McLaughlin (RM hereafter) effect in eclipsing binary stars (Rossiter 1924; McLaughlin 1924; Kopal 1999). Queloz et al. (2000) numerically computed the expected amplitude of such velocities, and put constraints on the stellar spin angular velocity and its direction angle with respect to the planetary orbit by comparing with the observed velocity anomalies.

Obviously this methodology provides unique and fundamental clues to understanding the formation process of extrasolar planetary systems. Planets are supposed to form in the proto-planetary disk surrounding the proto-star (e.g., Pollack et al. 1996). Thus the stellar spin and the planetary orbital axes are expected to be aligned. In turn any constraints on their (mis)alignment degree are useful clues to the origin of the angular momentum of planets and its subsequent evolution during possible migration of the planets into the close-in-orbits (e.g., Lin et al. 1996). In order to improve the reliability and precision of such results, analytical templates are of great value. In this paper, we show analytic formulae for radial velocities of transiting extrasolar planets. Those formulae may be used as standard templates in constraining a set of parameters for numerous transiting planets that will be detected in near future with *Corot* and *Kepler*.

The rest of the paper is organized as follows; §2 introduces a variety of parameters which characterize the dynamics of a planetary system and summarizes the radial velocity

curve neglecting the transit effect (or equivalently for a non-rotating star). Section 3 shows the radial a general theoretical framework of the RM effect for a star during the planetary transit. Sections 4 and 5 derive analytic expressions for radial velocity curves; in §4, we consider an idealistic case of the stellar intensity model without limb darkening and derive the exact analytic expressions. Based on this, section §5 presents approximate formulae taking into account the stellar limb darkening effect. We apply these analytic templates to a transiting system, HD209458 in §6 and examine the sensitivity to the parameters of the system. Finally, §7 is devoted to main conclusions and discussion.

2. Radial velocity profile for a star with a non-transiting planet

A close-in extrasolar planet system may have multiple outer planets, but we focus here a system which is well approximated by a two-body problem, i.e., that consists of a central star (mass m_s) and a planet (mass m_p). Figure 1 shows the schematic configuration of the top-view of the planetary orbit. The radial velocity curve of the star in the Kepler orbit may be described as follows (e.g., Murray & Dermott 1999).

First note that in the strictly two-body problem, the orbit of the planet with respect to the star is simply written as

$$r_p = \frac{a(1 - e^2)}{1 + e \cos f}, \quad (1)$$

where a is the semi-major axis, e is the eccentricity and f is the true anomaly (angular coordinate measured from the pericenter direction). The true anomaly f is written in terms of the eccentric anomaly E defined through the circumscribed circle which is concentric with the orbital ellipse as

$$\cos f = \frac{\cos E - e}{1 - e \cos E}. \quad (2)$$

If one introduces the mean motion n from the orbital period P_{orb} of the system as

$$n \equiv \frac{2\pi}{P_{\text{orb}}}, \quad (3)$$

then E is related to the mean anomaly M as (Kepler's equation)

$$M = E - e \sin E, \quad (4)$$

where $M \equiv n(t - \tau)$ with τ being the time of pericenter passage.

Using the parameters defined above, the radial velocity of the star along the line-of-sight of the observer (see Fig. 1) is written as (e.g., Murray & Dermott 1999)

$$v_{\text{rad,s}} = -\frac{m_p}{m_s + m_p} \frac{na \sin i}{\sqrt{1 - e^2}} [\sin(f + \varpi) + e \sin \varpi], \quad (5)$$

where i denotes the inclination angle between the direction normal to the orbital plane and the observer's line-of-sight, and we define $-\varpi$ as the longitude of the line-of-sight with respect to the pericenter (Fig.1). While f is not directly written as a function of the observer's time t , it is useful to rewrite equation (5) explicitly in terms of $M = n(t - \tau)$ even in an approximate manner. For this purpose, one can use the following expansions with respect to the eccentricity e (e.g., Murray & Dermott 1999):

$$\begin{aligned} \sin f &= 2\sqrt{1 - e^2} \sum_{k=1}^{\infty} \frac{1}{k} \frac{d}{de} J_k(ke) \sin kM \\ &= \sin M + e \sin 2M + e^2 \left(\frac{9}{8} \sin 3M - \frac{7}{8} \sin M \right) + O(e^3), \end{aligned} \quad (6)$$

$$\begin{aligned} \cos f &= -e + \frac{2(1 - e^2)}{e} \sum_{k=1}^{\infty} J_k(ke) \cos kM \\ &= \cos M + e(\cos 2M - 1) + \frac{9e^2}{8}(\cos 3M - \cos M) + O(e^3). \end{aligned} \quad (7)$$

Then equation (5) up to $O(e)$ should read

$$v_{\text{rad,s}} \approx -\frac{m_p na \sin i}{m_s + m_p} [\sin(M + \varpi) + e \sin(2M + \varpi)]. \quad (8)$$

3. Radial velocity profile for a star with a transiting planet

An occultation of a part of the rotating stellar surface during transit of the planet causes a time-dependent asymmetric feature in stellar emission/absorption line profiles. If the line profile is not well resolved, the asymmetry results in an apparent shift of the central line position which contributes to the overall “observed” stellar radial velocity additionally. In order to describe the effect quantitatively, we set the coordinate system centered at the star so that its y -axis is directed toward the observer (Fig.2). The z -axis is chosen so that the stellar rotation axis lies on the yz -plane. We also define the angle λ between z -axis and the normal vector \hat{n}_p of the planetary orbit plane projected on the xz -plane (Fig.3), i.e.,

$$\hat{n}_p = \begin{pmatrix} \sin \lambda \sin i \\ \cos i \\ \cos \lambda \sin i \end{pmatrix}. \quad (9)$$

Then the position of the planet is given by

$$\begin{aligned}\mathbf{X} &= R_y(\lambda)R_x\left(i - \frac{\pi}{2}\right)R_z\left(\varpi + \frac{\pi}{2}\right) \begin{pmatrix} r_p \cos f \\ r_p \sin f \\ 0 \end{pmatrix} \\ &= r_p \begin{pmatrix} -\cos \lambda \sin(f + \varpi) - \sin \lambda \cos i \cos(f + \varpi) \\ \sin i \cos(f + \varpi) \\ \sin \lambda \sin(f + \varpi) - \cos \lambda \cos i \cos(f + \varpi) \end{pmatrix},\end{aligned}\quad (10)$$

where $R_k(\theta)$ denotes the rotation matrix of an angle θ around the k -axis.

In our configuration, the angular velocity of the star is given as

$$\boldsymbol{\Omega}_s = (0, \Omega_s \cos I_s, \Omega_s \sin I_s). \quad (11)$$

Then the velocity of a point $\mathbf{R} = (x, y, z)$ on the stellar surface is

$$\mathbf{v} = \boldsymbol{\Omega}_s \times \mathbf{R} = \Omega_s \begin{pmatrix} z \cos I_s - y \sin I_s \\ x \sin I_s \\ -x \cos I_s \end{pmatrix}. \quad (12)$$

Thus the radiation at frequency ν from that point suffers from the Doppler shift due to the stellar rotation by an amount of

$$\frac{\Delta\nu}{\nu} = \frac{\Omega_s x \sin I_s}{c} \quad (13)$$

with respect to the observer located along the y -axis in the present case.

Consider a specific (emission or absorption) line whose intensity at a point (x, z) on the projected stellar surface is given by $I_\nu(x, z) = I(x, z)H(\nu)$, where $H(\nu)$ represents the line profile. The observed flux is computed by integrating the Doppler-shifted intensity at each point over the entire (projected) surface of the star:

$$F_\nu = \int \left(1 + \frac{\Delta\nu}{\nu}\right)^3 I(x, z)H(\nu - \Delta\nu) \frac{dx dz}{D^2}, \quad (14)$$

where D is the distance between the star and the observer. The factor $(1 + \Delta\nu/\nu)^3$ appears due to the Lorentz invariance of the quantity I_ν/ν^3 . While our analysis is applicable to both emission and absorption lines, we consider an emission line centered at $\nu = \nu_0$ in what follows just for definiteness. Then the line profile function satisfies

$$\int H(\nu) d\nu = 1, \quad (15)$$

$$\int \nu H(\nu) d\nu = \nu_0. \quad (16)$$

Since $H(\nu)$ is supposed to be sharply peaked only around ν_0 , we have approximately

$$\int f(\nu)H(\nu)d\nu \approx f(\nu_0), \quad (17)$$

for an arbitrary smooth function, $f(\nu)$.

If the resolution of the observational spectrograph were sufficiently high, the line profiles of the star and the planetary shadow would be separated, or at least the asymmetric feature might be detected for transiting systems (e.g., Charbonneau et al. 1998, 1999). In reality, however, such a high spectral resolution is quite demanding, and here we assume a somewhat lower resolution. Thus we simply compute the resulting time-dependent shift of the line profile weighted mean position $\bar{\nu}$ due to an asymmetric occultation of the stellar surface during the passage of the transiting planet. Using the expression (14) and the properties of line profile function (eqs. [15] to [17]), we obtain

$$\begin{aligned} \bar{\nu} &\equiv \frac{\int \nu F_\nu d\nu}{\int F_\nu d\nu} \\ &= \nu_0 \left\{ 1 + \frac{\iint \left(1 + \frac{\Delta\nu}{\nu_0}\right)^3 \frac{\Delta\nu}{\nu_0} I(x, z) dx dz}{\iint \left(1 + \frac{\Delta\nu}{\nu_0}\right)^3 I(x, z) dx dz} \right\}. \end{aligned} \quad (18)$$

Since the amplitude of the Doppler shift (eq.[13]) is small, one can safely expand $\bar{\nu}$ up to the leading order of $\Delta\nu/\nu$ as

$$\begin{aligned} \bar{\nu} &= \nu_0 \left\{ 1 + \frac{\iint \frac{\Delta\nu}{\nu_0} I(x, z) dx dz}{\iint I(x, z) dx dz} + \mathcal{O}\left(\frac{\Delta\nu^2}{\nu_0^2}\right) \right\} \\ &\approx \nu_0 \left\{ 1 + \frac{\Omega_s \sin I_s}{c} \frac{\iint x I(x, z) dx dz}{\iint I(x, z) dx dz} \right\}. \end{aligned} \quad (19)$$

Therefore the “apparent” radial stellar velocity anomaly due to the RM effect is expressed as

$$\Delta v_s = -\Omega_s \sin I_s \frac{\iint x I(x, z) dx dz}{\iint I(x, z) dx dz}. \quad (20)$$

Equation (20) is the basic relation between $I(x, z)$ and Δv_s in our subsequent analysis. Figure 4 shows a schematic illustration of the RM effect. Depending on the inclination and the orbital rotation direction relative to the stellar spin axis, the velocity curve anomaly due to the RM effect exhibits rather different behavior.

The remaining task is to evaluate the integrals adopting a certain model of a stellar surface intensity $I(x, z)$. Note that previous literatures in the analytical study of radial velocity curves focused on expressing the integrals in the radial velocity shift (20) in terms of Kopal's associated α -functions under some model assumptions of the stellar intensity (e.g., Hosokawa 1953; Kopal 1999). While such detailed and exact approaches are required for stellar eclipsing binaries, the evaluation of the α -function is a demanding numerical task. Furthermore for those systems a variety of effects become important including limb-darkening, distortion of stars due to their rotation and tidal interaction, reflection effect (heating by the radiant energy of the companion), and, gravity darkening (variation of the surface brightness due to the local surface gravity acceleration change). For the extrasolar planetary systems, on the other hand, the radius and mass of a planet are significantly smaller than those of the host star. Thus most of those effects can be safely neglected, and one can derive simpler, and still practically useful, analytical formulae applying perturbative expansion. In what follows, we present such analytic expressions for the RM effect with and without the stellar limb darkening.

4. Analytic expressions for a uniform stellar disk (without limb darkening)

As a step toward an analytic model for the RM effect for extrasolar planetary systems, let us consider first an idealistic case in which the limb darkening effect is neglected. We also assume that the planet is completely optically thick and not rotating, which is also assumed in the next section. In this case, one can obtain the exact analytic expression even without the perturbative expansion. The intensity at (x, z) on the uniform stellar surface becomes

$$I(x, z) = \begin{cases} I_0 & ; x^2 + z^2 \leq R_s^2 \text{ and } (x - X_p)^2 + (z - Z_p)^2 \geq R_p^2 \\ 0 & ; \text{otherwise} \end{cases}, \quad (21)$$

where $\mathbf{X}_p = (X_p, Y_p, Z_p)$ is the position of the center of the planet, and R_s and R_p denote the radii of the star and the planet, respectively. We evaluate equation (20) at complete transit, ingress and egress phases in the following subsections (see Fig.5).

4.1. Complete transit phase

During a complete transit phase, the position of the planet satisfies the relation $\sqrt{X_p^2 + Z_p^2} < R_s - R_p$. Thus, the range of the integral in equation (20) is simply given by the stellar surface area subtracted by the entire planetary disk, i.e.,

$$\iint dx dz \longrightarrow \int_{-R_s}^{R_s} dx \int_{-\sqrt{R_s^2 - x^2}}^{\sqrt{R_s^2 - x^2}} dz - \int_{X_p - R_p}^{X_p + R_p} dx \int_{Z_p - \sqrt{R_p^2 - (x - X_p)^2}}^{Z_p + \sqrt{R_p^2 - (x - X_p)^2}} dz. \quad (22)$$

Then we obtain

$$\iint I(x, z) dx dz = \pi(R_s^2 - R_p^2) I_0, \quad (23)$$

$$\iint x I(x, z) dx dz = -X_p \pi R_p^2 I_0. \quad (24)$$

Substituting these results into equation (20), we find

$$\Delta v_s = \Omega_s X_p \sin I_s \frac{\gamma^2}{1 - \gamma^2} \quad \left(\gamma \equiv \frac{R_p}{R_s} \right). \quad (25)$$

Equation (25) implies that the time dependence of the RM effect during the complete transit is entirely incorporated in the planet position, i.e., $X_p = X_p(t)$.

4.2. Ingress and egress phases

At ingress and egress phases, on the other hand, the location of the planet satisfies the relation, $R_s - R_p < \sqrt{X_p^2 + Z_p^2} < R_s + R_p$. Just for computational convenience, we rotate the coordinate in a time-dependent manner so that the planet is always located along the new x -axis:

$$\begin{pmatrix} \tilde{x} \\ \tilde{z} \end{pmatrix} = \frac{1}{R_s \sqrt{X_p^2 + Z_p^2}} \begin{pmatrix} X_p & Z_p \\ -Z_p & X_p \end{pmatrix} \begin{pmatrix} x \\ z \end{pmatrix}. \quad (26)$$

Then the position of the planet is given by

$$\begin{pmatrix} \tilde{X}_p \\ \tilde{Z}_p \end{pmatrix} = \begin{pmatrix} 1 + \eta_p \\ 0 \end{pmatrix}, \quad (27)$$

where

$$\eta_p = \frac{\sqrt{X_p^2 + Z_p^2}}{R_s} - 1. \quad (28)$$

In the new coordinate, equation (21) is rewritten as

$$I(\tilde{x}, \tilde{z}) = \begin{cases} I_0 & ; \tilde{x}^2 + \tilde{z}^2 \leq 1 \text{ and } (\tilde{x} - 1 - \eta_p)^2 + \tilde{z}^2 \geq \gamma^2 \\ 0 & ; \text{otherwise} \end{cases}, \quad (29)$$

and the moments of the intensity reduce to

$$\iint I(x, z) dx dz = R_s^2 \left\{ \pi - \iint_S I(\tilde{x}, \tilde{z}) d\tilde{z} d\tilde{x} \right\}, \quad (30)$$

$$\iint x I(x, z) dx dz = -\frac{R_s^2}{1 + \eta_p} \iint_S (X_p \tilde{x} - Z_p \tilde{z}) I(\tilde{x}, \tilde{z}) d\tilde{z} d\tilde{x}, \quad (31)$$

where the range of the integrals denoted by S indicates the overlapping region between the stellar and the planetary disks and may be explicitly written as (*dark-shaded* in Fig. 6):

$$\iint_S d\tilde{z} d\tilde{x} \rightarrow \int_{x_0}^1 d\tilde{x} \int_{-\sqrt{1-\tilde{x}^2}}^{\sqrt{1-\tilde{x}^2}} d\tilde{z} + \int_{\tilde{X}_p - \gamma}^{x_0} d\tilde{x} \int_{-\sqrt{\gamma^2 - (\tilde{x} - \tilde{X}_p)^2}}^{\sqrt{\gamma^2 - (\tilde{x} - \tilde{X}_p)^2}} d\tilde{z}. \quad (32)$$

Note that the planetary and stellar circles intersect at $(x_0, \pm z_0)$, where

$$x_0 = 1 - \frac{\gamma^2 - \eta_p^2}{2(1 + \eta_p)}, \quad z_0 = \sqrt{1 - x_0^2} = \frac{\sqrt{(\gamma^2 - \eta_p^2)[(\eta_p + 2)^2 - \gamma^2]}}{2(1 + \eta_p)}. \quad (33)$$

Let us also introduce

$$\zeta \equiv 1 + \eta_p - x_0 = \frac{2\eta_p + \gamma^2 + \eta_p^2}{2(1 + \eta_p)}. \quad (34)$$

Physically speaking, this corresponds to the separation between the intersection and the center of planet along the \tilde{X} axis, but we define that ζ can be negative (see Fig. 6) as well. Then equations (30) and (31) are analytically integrated as

$$\iint_S I(\tilde{x}, \tilde{z}) d\tilde{z} d\tilde{x} = I_0 \left[\sin^{-1} z_0 - (1 + \eta_p) z_0 + \gamma^2 \cos^{-1}(\zeta/\gamma) \right], \quad (35)$$

and

$$\iint_S (\tilde{x} X_p - \tilde{z} Z_p) I(\tilde{x}, \tilde{z}) d\tilde{z} d\tilde{x} = I_0 X_p (1 + \eta_p) \left[-z_0 \zeta + \gamma^2 \cos^{-1}(\zeta/\gamma) \right], \quad (36)$$

respectively.

Combining these results, we finally find that equation (20) reduces to

$$\Delta v_s = \Omega_s X_p \sin I_s \frac{-z_0 \zeta + \gamma^2 \cos^{-1}(\zeta/\gamma)}{\pi - \sin^{-1} z_0 + (1 + \eta_p) z_0 - \gamma^2 \cos^{-1}(\zeta/\gamma)}. \quad (37)$$

While the above expression for Δv_s seems complicated a bit, this is the exact result for the radial velocity anomaly through the relations (28), (33) and (34) in terms of the planet position (X_p, Z_p) specified by equation (10).

5. Effect of the stellar limb darkening

To be more realistic, we now take account of the effect of limb darkening which produces the radial dependence of the intensity on the stellar disk. Among various models proposed so far (e.g., Claret 2000), we adopt a linear limb darkening law as the simplest but practically realistic one. Introducing the linear limb darkening coefficient ϵ , the stellar intensity is now given by

$$I(x, z) = \begin{cases} I_0 \{1 - \epsilon(1 - \mu)\} & ; \quad x^2 + z^2 \leq R_s^2 \text{ and } (x - X_p)^2 + (z - Z_p)^2 \geq R_p^2 \\ 0 & ; \text{ otherwise} \end{cases}, \quad (38)$$

where μ is the cosine of the angle between the line-of-sight and the normal to the local stellar surface :

$$\mu = \sqrt{1 - \frac{x^2 + z^2}{R_s^2}}. \quad (39)$$

With the limb darkening effect, however, equation (20) can no longer be analytically integrated in an exact manner. So we will construct approximate analytical formulae on the basis of the result without limb darkening ($\epsilon = 0$; see section 4).

5.1. Complete transit phase

Applying the analytic results of §4.1 to the stellar intensity model (38), equation (20) is formally rewritten as

$$\Delta v_s = \Omega_s X_p \sin I_s \frac{\gamma^2 \{1 - \epsilon(1 - W_2)\}}{1 - \gamma^2 - \epsilon \left\{ \frac{1}{3} - \gamma^2(1 - W_1) \right\}}, \quad (40)$$

where W_1 and W_2 are defined as

$$W_1 = \frac{1}{\pi R_p^2} \iint_S dx dz \sqrt{1 - (x^2 + z^2)/R_s^2}, \quad (41)$$

$$W_2 = \frac{1}{X_p \pi R_p^2} \iint_S dx dz x \sqrt{1 - (x^2 + z^2)/R_s^2}. \quad (42)$$

The above integrals are carried out over the entire planetary disk. As discussed in Appendix A.1, they reduce to one-dimensional integrals, which can be expanded with respect to $\gamma = R_p/R_s$. Specifically, equations (A10) and (A14) shows perturbative expressions up to the fourth order in γ . The accuracy of the fourth order perturbation expansion is within a few percent level even for $\gamma \sim 0.3$ (Fig.15). In practice, however, the value of γ is expected to

be much smaller, $\gamma \lesssim 0.1$. In this case, higher-order terms in equations (A10) and (A14) contribute merely $\sim 1\%$ to equation (40) and one can safely use

$$W_1(\rho) \simeq 0, \quad (43)$$

$$W_2(\rho) \simeq (1 - \rho^2)^{1/2}, \quad (44)$$

where $\rho \equiv \sqrt{X_p^2 + Z_p^2}/R_s$ ($0 < \rho < 1 - \gamma$).

5.2. Ingress and egress phases

If linear limb darkening effect is taken into account, equation (37) describing ingress and egress phases now becomes

$$\begin{aligned} \Delta v_s &= \Omega_s X_p \sin I_s \\ &\quad (1 - \epsilon) \{ -z_0 \zeta + \gamma^2 \cos^{-1}(\zeta/\gamma) \} + \frac{\epsilon}{1 + \eta_p} W_4 \\ &\quad \times \frac{\pi (1 - \frac{1}{3}\epsilon) - (1 - \epsilon) \{ \sin^{-1} z_0 - (1 + \eta_p) z_0 + \gamma^2 \cos^{-1}(\zeta/\gamma) \} - \epsilon W_3}{\pi (1 - \frac{1}{3}\epsilon) - (1 - \epsilon) \{ \sin^{-1} z_0 - (1 + \eta_p) z_0 + \gamma^2 \cos^{-1}(\zeta/\gamma) \} - \epsilon W_3}, \end{aligned} \quad (45)$$

where W_3 and W_4 are defined by

$$W_3 = \iint_S d\tilde{x} d\tilde{z} \sqrt{1 - \tilde{x}^2 - \tilde{z}^2}, \quad (46)$$

$$W_4 = \iint_S d\tilde{x} d\tilde{z} \tilde{x} \sqrt{1 - \tilde{x}^2 - \tilde{z}^2}. \quad (47)$$

Appendix A.2 derives approximate analytic expressions (A23) and (A24) for equations (46) and (47), respectively, assuming that $\gamma \ll 1$. Again if $\gamma \lesssim 0.1$, they can be safely set as

$$W_3 \simeq 0, \quad (48)$$

$$W_4 \simeq \frac{\pi}{2} \gamma(\gamma - \zeta) x_c \frac{g(x_c; \eta_p, \gamma)}{g(1 - \gamma; -\gamma, \gamma)} W_2(1 - \gamma), \quad (49)$$

where

$$x_c = x_0 + \frac{\zeta - \gamma}{2}, \quad (50)$$

$$\begin{aligned} g(x; \eta_p, \gamma) &= (1 - x^2) \sin^{-1} \left\{ \frac{\gamma^2 - (x - 1 - \eta_p)^2}{1 - x^2} \right\}^{1/2} \\ &\quad + \sqrt{\{\gamma^2 - (x - 1 - \eta_p)^2\} \{1 - x^2 - \gamma^2 + (x - 1 - \eta_p)^2\}}. \end{aligned} \quad (51)$$

As shown in Figure 16, the accuracy of equations (48) and (49) is typically within a fractional error of $5 \sim 10$ percent. Nevertheless their contribution to the total error budget for the velocity anomaly (45) is within a few percent level (see §6.2). Thus equations (48) and (49) are practically good approximations in most cases.

6. Application to the HD209458 system

So far HD209458 is the only extrasolar planetary system in which the RM effect is detected; Queloz et al. (2000) reported the first detection of this effect with ELODIE spectrograph on the 193 cm telescope of the Observatoire de Haute Provence. They numerically computed the radial velocity anomaly due to the RM effect for a variety of model parameters, and compared with the observed radial curves. They concluded that $\alpha = \pm 3.9_{-21}^{+18}$ deg and $V \sin I_s = 3.75 \pm 1.25$ km s $^{-1}$, where α is the angle between the planet's orbital plane and the star's apparent equatorial plane and V denotes the stellar surface velocity. They are written as $\alpha = \cos^{-1}(\sin i \cos \lambda)$ and $V = R_s \Omega_s$ according to the notation of our current paper. We summarize the current estimates of the stellar and planetary parameters for HD209458 in Table 2, and the best solution for the spin parameters by Queloz et al. (2000) in Table 3, respectively. Since HD209458 still remains as the currently best target for the precise measurement of the RM effect, we will consider in this section the extent to which one can improve the constraints on the spin parameters with our analytic formulae.

6.1. Parameter dependence

Adopting the linear limb darkening law for the stellar intensity model, the RM effect for a system in the Keplerian orbit is specified by 10 parameters; the limb darkening coefficient ϵ , the orbital parameters of the system (a , e , i , ϖ , P_{orb}), the size of the stellar and the planet disks (R_s , R_p), the projected stellar surface velocity $V \sin I_s$, and finally the projected angle between the stellar spin axis and the normal direction of the orbital plane λ . Except the last two parameters ($V \sin I_s$ and λ), the other eight parameters may be independently determined from the usual radial velocity and transiting photometric data, at least in principle. This is indeed the case for the HD209458 system (see Table 2). Therefore it is natural to ask the extent to which one can put constraints on the two parameters, $V \sin I_s$ and λ from the radial velocity anomaly during the transit due to the RM effect.

Consider first the sensitivity to the spin parameters ($V \sin I_s$, λ). Figures 7 and 8, illustrate our approximations for Δv_s adopting the estimated parameters of the HD209458 system (Table 2) with and without the stellar limb darkening (i.e., $\epsilon = 0$ and 0.64 to be specific), respectively. The central transit epoch is chosen as $t = 0$. Then ingress starts at $t = -1.55$ hr, the complete transit lasts for $-1.07 < t < 1.08$ hr, and egress ends at $t = 1.56$ hr for $e = 0.1$ (sometimes these four epochs are referred to as the first, second, third and fourth contacts, respectively). The range of the spin parameters, $V \sin I_s$ and λ adopted in these figures roughly cover the uncertainties of the values of Queloz et al. (2000).

Comparison of the two figures indicates that the radial velocity anomaly Δv_s is also sensitive to the linear limb darkening coefficient ϵ . Obviously the amplitude of the radial velocity shift Δv_r is sensitive to $V \sin I_s$. The projected angle λ shifts the zero-point of the radial velocity anomaly at earlier ($\lambda > 0$) and later ($\lambda < 0$) epochs for the orbital inclination $i < 90^\circ$. This produces an asymmetry of the shape of the radial velocity anomaly. Note that the behavior becomes opposite for the inclination $i > 90^\circ$, corresponding to the parameter degeneracy between (i, λ) and $(180^\circ - i, -\lambda)$. Because of the different dependence of the overall radial velocity anomaly on the spin parameters ($V \sin I_s, \lambda$), one may put more stringent constraints on those if combined with future precision data attainable by 8–10 m class telescopes with high dispersion spectrograph such as Subaru HDS.

Before addressing this issue in detail, it would be helpful to clarify the dependence of the RM effect on the other remaining parameters. To investigate this, we quantify the variation of radial velocity shift with respect to a specific parameter change $p \sim p + dp$ by

$$\delta \Delta v_s \equiv \lim_{dp \rightarrow 0} \frac{\Delta v_s(p + dp) - \Delta v_s(p)}{dp/p} \quad (52)$$

for $p = (a, R_s, R_p, P_{\text{orb}}, V \sin I_s, \epsilon, e)$. In practice, we systematically decrease the value of dp/p for each parameter down to 10^{-6} , and ensure the convergence of the derivative. For the angular parameters $p = (i, \varpi, \lambda)$, we simply take their scaling values at 10° :

$$\delta \Delta v_s \equiv \lim_{dp \rightarrow 0} \frac{\Delta v_s(p + dp) - \Delta v_s(p)}{dp/10^\circ}. \quad (53)$$

Here, we confirm the convergence of the derivative by decreasing the value of $dp/10^\circ$ down to 10^{-6} in these cases. Our analytic formulae are indeed useful in evaluating these quantities at the fiducial parameters of the HD209458 system (Tables 2 and 3). The results are plotted in Figure 9 as a function of time. Note that our definition of $\delta \Delta v_s$ is *normalized* by the fractional error in parameter, i.e., dp/p .

Figure 9 clearly shows that the stellar radius R_s and the orbital parameters a, i and P_{orb} sensitively change the normalized radial velocity variation $\delta \Delta v_s$ at ingress and egress phases, while the spin parameters ($V \sin I_s, \lambda$) have a relatively smaller effect on $\delta \Delta v_s$. To quantify the actual deviation of the radial velocity shift caused by the systematic errors in observation, we must multiply the observational uncertainty listed in Table 2. Then, it turns out that the most sensitive parameter is $V \sin I_s$ causing the 12 m s^{-1} variation of the radial velocity shift. The other parameters change the the radial velocity shift at ingress and egress phases by less than 5 m s^{-1} . This amplitude itself is comparable to $\delta \Delta v_s$ induced by the uncertainty of the projected angle λ . Nevertheless the different time-dependent effect of the various parameters may be used to break the parameter degeneracy, which

would enable an accurate determination of the spin parameters λ and $V \sin I_s$. In addition, Figure 9 even suggests that a more precise determination of the orbital parameters other than spin parameters is also possible by combining the RM effect with usual radial velocity measurement.

6.2. Accuracy of our formulae

While our analytical formulae presented in the previous section will improve the efficiency of parameter estimations relative to fully numerical approaches, we have to address a couple of issues before applying to real data; their accuracy and the effect of the finite exposure time. Our formulae with limb darkening are derived on the basis of an empirical approximation to the integrals of the stellar surface intensity (§5). Furthermore the real data do not instantaneously sample the radial velocity, but are averaged over a finite exposure time. We will directly test those effects against the numerical solutions of equation (20). Figures 10 and 11 compare three results; numerical integration of equation (20), our analytic formulae, and numerically average of equation (20) over $\Delta t = 10$ min exposure time (in practice, we separately average the denominator and the numerator of the analytic formulae assuming $\Delta t = 10$ min, and then take their ratio). They are labeled A, B, and C, and plotted in solid, dotted, and dashed, respectively, in the upper panels.

For $\epsilon = 0$, the analytic formulae (curve B) are exact, and the completely negligible difference A–B should be regarded as a welcome check of the accuracy of our numerical integration scheme. The lower panels suggest that the three results agree within an accuracy of $\sim 1\text{m s}^{-1}$ which is below a typical radial velocity sensitivity achieved ($\sim 3\text{m s}^{-1}$), and is only comparable to the latest achievement by HARPS (Santos et al. 2004). Therefore as far as the HD209458 system is concerned, we can safely use our analytic formulae as useful templates for the RM effect even if the finite exposure time of an order of 10 min is taken into account.

6.3. Mock analysis of the spin parameter estimation

Now we are in a position to ask if our formulae combined with precision spectroscopic data can improve the previous constraints on the spin parameters ($\Omega_s \sin I_s$, λ) among others. For this purpose, we create mock data for the radial velocity anomaly of the HD209458 system and fit them to the analytic formulae. Basically, the mock data were created adopting the central values of the parameters listed in Tables 2 and 3, but assigned the overall Gaussian

random error of the rms amplitude 5 m s^{-1} , which is the level of precision achieved with the Subaru High Dispersion Spectrograph (HDS) assuming the exposure time of $\Delta t = 10$ minutes (Winn et al. 2004). In the light of the most recent sensitivity achieved by HARPS (Santos et al. 2004) ($\sim 1 \text{ m s}^{-1}$), our error assignment may be still conservative if the error is not dominated by other possible systematics. To mimic the effect of the finite exposure time, we numerically integrate the denominator and the numerator of equation (20) separately over $\Delta t = 10\text{min}$. Then we take the ratio, and assign the random error as mentioned above.

Note that the number of independent data points during the transit phase (~ 3 hrs including ingress and egress phases) is 16 for $\Delta = 10$ min. The generated mock data are then fitted to the analytic radial velocity anomaly to estimate the spin parameters. Here, the fitting is performed assuming the prior knowledge of the remaining 8 parameters.

First let us see how the spin parameters are reliably estimated from the χ^2 -fit. To examine this, we create 50,000 mock realizations and calculate the joint probability distribution of the best-fit parameters under a certain prior knowledge of R_s , R_p and a . We use the χ^2 function:

$$\chi^2(V \sin I_s, \lambda) = \sum_{i=1}^N \left\{ \frac{\Delta v_{s,i}^{\text{data}} - \Delta v_s^{\text{model}}(V \sin I_s, \lambda; t_i)}{\sigma_{\Delta v}} \right\}^2 \quad (54)$$

with $\sigma_{\Delta v} = 5 \text{ m s}^{-1}$ and $N = 16$. In this analysis, according to the result in Figure 9, we particularly focus on the five parameters; $V \sin I_s$, λ , R_s , R_p and a . Their input values are 3750 m s^{-1} , 0° , $1.146 R_\odot$, $1.347 R_J$ and 0.0468 AU , respectively. We assume a set of different prior values for R_s , R_p and a indicated in each panel of Figure 12, and then perform the χ^2 -minimization over $V \sin I_s$ and λ .

The results are plotted as contour levels in Figure 12. Here, the two contour curves in each panel represent the 1- and 2- σ levels of the joint probability. The solid curves plotted along the horizontal and the vertical axes are the probability distribution of $V \sin I_s$ and λ , respectively, each of which is the projection of the joint probability distribution over the other parameter. Note that in both cases, the probability distribution is well approximated by the Gaussian distribution with 1- σ values of $\sigma_{V \sin I_s} \simeq 310 \text{ m s}^{-1}$ and $\sigma_\lambda \simeq 3.4^\circ$. This result indicates that the estimated value for $V \sin I_s$ is rather sensitive to the assumed value of the planetary radius R_p , while λ can be estimated reliably even if R_p is not known accurately. This comes from the fact that the velocity shift is roughly proportional to $V \sin I_s R_p^2$, however the projected angle λ is sensitive only to the asymmetry of the radial velocity shift curve. Another important aspect is that the uncertainty of the prior knowledge for stellar radius has little effect on the parameter estimation.

The above analysis implies that with suitably short exposure time, our formulae provide an unbiased estimation of the spin parameters *statistically* if we have reasonably accurate

prior knowledge of the other parameters of the system. In reality, however, it may be more relevant to ask the reliability of the confidence level of the spin parameters derived from *a single realization* rather than the 50,000 realizations. This is related to the above analysis statistically, but maybe it is more appropriate to the situation that one encounters in any observation. For this purpose, we randomly select one from the 50,000 realizations, and compute 1σ and 2σ confidence contours from the *relative* confidence levels:

$$\Delta\chi^2 \equiv \chi^2(V \sin I_s, \lambda) - \chi^2(V \sin I_{s,0}, \lambda_0), \quad (55)$$

where $V \sin I_{s,0}$ and λ_0 are the best-fit values. Figure 13 shows the estimated parameter regions on $V \sin I_s$ versus λ plane, and the best-fit values are indicated by the symbol “+” in each panel. The corresponding radial velocity curves are depicted in Figure 14, together with both the best-fit and the true curves (*solid* and *dashed*).

Basically, Figure 13 demonstrates that the spin parameters $V \sin I_s$ and λ can be constrained around the best-fit values with the 1σ errors of $\Delta V \sin I_s \simeq \pm 300 \text{ m s}^{-1}$ and $\Delta\lambda \simeq \pm 4^\circ$, which greatly improves the uncertainties (by a factor of 4) relative to the previous result by Queloz et al. (2000) (see Table 3).

7. Conclusions and discussion

We have discussed a methodology to estimate the stellar spin angular velocity and its direction angle with respect to the planetary orbit for transiting extrasolar planetary systems using the RM effect previously known in eclipsing binary stars (Rossiter 1924; McLaughlin 1924; Kopal 1999). In particular we have derived analytic expressions of the radial velocity anomaly, Δv_s , which are sufficiently accurate for extrasolar planetary systems. If the stellar limb darkening is neglected, the expression is exact. We have extended the result to the case with limb darkening and obtained approximate but accurate analytic formulae. For a typical value of $\gamma = R_p/R_s \sim 0.1$, the formulae reduce to a simple form (eqs.[40], [43], [44], [45], [48], and [49]):

$$\Delta v_s = \Omega_s X_p \sin I_s \frac{\gamma^2 \{1 - \epsilon(1 - W_2)\}}{1 - \gamma^2 - \epsilon \left\{ \frac{1}{3} - \gamma^2 \right\}} \quad (56)$$

during the complete transit phase and

$$\Delta v_s = \Omega_s X_p \sin I_s \frac{(1 - \epsilon) \{-z_0\zeta + \gamma^2 \cos^{-1}(\zeta/\gamma)\} + \frac{\epsilon}{1 + \eta_p} W_4}{\pi \left(1 - \frac{1}{3}\epsilon\right) - (1 - \epsilon) \{\sin^{-1} z_0 - (1 + \eta_p)z_0 + \gamma^2 \cos^{-1}(\zeta/\gamma)\}} \quad (57)$$

during the egress/ingress phases, where

$$W_2 = \frac{(R_s^2 - X_p^2 - Z_p^2)^{1/2}}{R_s}, \quad (58)$$

$$W_4 = \frac{\pi}{2} \gamma^{3/2} (2 - \gamma)^{1/2} (\gamma - \zeta) x_c \frac{g(x_c; \eta_p, \gamma)}{g(1 - \gamma; -\gamma, \gamma)}, \quad (59)$$

with $g(x; a, b)$ being equation (A17). The definition and the meaning of the variables in the above expressions are summarized in Table 1.

The numerical accuracy of the above formulae was checked using a specific example of the transiting extrasolar planetary system, HD209458, and we found that they are accurate within a few percent. Our analytic formulae for the radial velocity anomaly are useful in several ways; one can estimate the planetary parameters much more efficiently and easily since one does not have to resort to computationally demanding numerical modeling. Furthermore the resulting uncertainties of the fitted parameters and their correlations are easily evaluated. To illustrate these advantages specifically, we performed a parameter estimation applying the formulae against mock data for HD209458. We showed that with precision data obtainable by 8–10 m class telescopes such as Subaru HDS, our formulae improve the efficiency and robustness of estimating the spin parameters, $V \sin I_s$ and λ . Furthermore the combined data analysis with the asteroseismology (e.g., Gizon & Solanki 2003) and/or the correlation between the mean level activity of emission and the rotation period (e.g., Noyes et al. 1985) may break the degeneracy between V and I_s in extrasolar planetary systems.

Among recently discovered transiting extrasolar planetary systems, i.e., TrES-1 by Trans-Atlantic Exoplanet Survey (Alonso et al. 2004) and OGLE-TR-33, 56, 111, 113, 132 by Optically Gravitational Lens Event survey (Bouchy et al. 2004), TrES-1 seems to be very similar to the HD209458 system. Thus it is an interesting target to determine the spin parameters via the RM effect; if its planetary orbit and the stellar rotation share the same direction as discovered for the HD209458 system, it would be an important confirmation of the current view of the planet formation out of the proto-planetary disk surrounding the proto-star. If not, the result would be more exciting and even challenge the standard view, depending on the value of the misalignment angle λ .

We also note that the future satellites, *Corot* and *Kepler*, will detect numerous transiting planetary systems, most of which will be important targets for the RM effect in 8 - 10 m class ground-based telescopes. We hope that our analytic formulae presented here will be a useful template in estimating parameters for those stellar and planetary systems.

Finally it is interesting to note that the RM effect may be even used as yet another new detection method of transiting planetary systems. For the HD209458 system, the stellar

radial velocity amplitude due to the Kepler motion is around 100 m s^{-1} . Since the stellar rotation velocity is around 4 km s^{-1} , the maximum radial velocity anomaly due to the RM effect is $\sim 40(\gamma/0.1)^2 \text{ m s}^{-1}$ and thus is very close to the former. On the other hand, the latter could be significantly larger if the host star rotates faster, and/or the host star (the planet) has a smaller (larger) radius. In extreme cases, the radial velocity curve, with a periodicity of a few days for instance, is barely detectable, but the velocity anomaly is quite visible for a few hours of transiting phase. So the conventional radial velocity curve analysis might have missed some of the potentially interesting spectroscopic signature of transiting planets. A search for such specific signatures deserves trying against existing or future spectroscopic samples which do not show any clear conventional feature of radial velocity periodicity.

In conclusion, we have demonstrated that the radial velocity anomaly due to the RM effect provides a reliable estimation of spin parameters. Combining with the analytic formulae for radial velocity shift Δv_s , this methodology becomes a powerful tool in extracting information on the formation and the evolution of extrasolar planetary systems, especially the origin of their angular momentum. Although unlikely, we may even speculate that a future RM observation may discover an extrasolar planetary system in which the stellar spin and the planetary orbital axes are anti-parallel or orthogonal. Then it would have a great impact on the planetary formation scenario, which has to invoke the additional effect from possible other planets in the system during the migration or the capture of a free-floating planet. While it is premature to discuss such extreme possibilities at this point, the observational exploration of transiting systems using the RM effect is one of the most important probes to better understanding of the origin of extrasolar planets.

We thank Christopher Leigh, Norio Narita, and Edwin Turner for useful discussions and comments. We are also grateful to Didier Queloz for providing the ELODIE data of the radial velocity of HD209458. This work is supported in part by a Grant-in-Aid for Scientific Research from the Japan Society for Promotion of Science (No.12640231, 14740157).

A. Approximation of integrals

In this appendix, the approximate expressions for the integrals W_i ($i = 1 \sim 4$) defined in section 5 are derived. Below, we present the results separately for the integrals W_1 and W_2 in appendix A.1 and for W_3 and W_4 in appendix A.2.

A.1. Integrals W_1 and W_2

First consider the integral W_1 . For further reduction of the integral, it is convenient to rewrite equation (41) in terms of the new variables:

$$(x, z) = R_p \sigma(\cos \varphi, \sin \varphi) + (X_p, Z_p), \quad (X_p, Z_p) = R_s \rho(\cos \theta, \sin \theta). \quad (\text{A1})$$

Then we obtain

$$W_1 = \frac{1}{\pi} \int_0^1 d\sigma \int_0^{2\pi} d\varphi \sigma \sqrt{1 - \rho^2 \sin^2(\theta - \varphi) - \{\gamma\sigma + \rho \cos(\theta - \varphi)\}^2}. \quad (\text{A2})$$

Here, the variable ρ runs from 0 to $1 - \gamma$. In the above expression, the integral over σ is analytically expressed, a part of which is further integrated out. The resultant expression becomes

$$W_1 = \frac{2}{3\gamma^2} (1 - \rho^2)^{1/2} \left(1 - \frac{1}{4}\rho^2 \right) - w_A + w_B, \quad (\text{A3})$$

where w_A and w_B are given by

$$w_A = \frac{1}{\pi\gamma^2} \left[\frac{1}{3} \int_0^{2\pi} d\varphi (1 - \rho^2 - \gamma^2 - 2\rho\gamma \cos \varphi)^{3/2} + \frac{1}{2} \int_0^{2\pi} d\varphi (\rho^2 \cos \varphi + \rho\gamma) \cos \varphi (1 - \rho^2 - \gamma^2 - 2\rho\gamma \cos \varphi)^{1/2} \right], \quad (\text{A4})$$

$$w_B = \frac{1}{2\pi\gamma^2} \int_0^{2\pi} d\varphi \rho \cos \varphi (1 - \rho^2 \sin^2 \varphi) \times \left\{ \sin^{-1} \left(\frac{\rho \cos \varphi}{\sqrt{1 - \rho^2 \sin^2 \varphi}} \right) - \sin^{-1} \left(\frac{\gamma + \rho \cos \varphi}{\sqrt{1 - \rho^2 \sin^2 \varphi}} \right) \right\}. \quad (\text{A5})$$

Note that the integrals w_A and w_B are analytically expressed in terms of the complete elliptic integrals of the first kind, $K(m)$, the second kind, $E(m)$, and the third kind, $\Pi(n, m)$:

$$w_A = \frac{1}{45\pi\gamma^4} \{1 - (\gamma + \rho)^2\}^{1/2} \times \left[\{3(1 - \rho^2)^2 - \gamma^2(71 - 17\rho^2) + 68\gamma^4\} E(m) \right.$$

$$-\{(\gamma - \rho)^2 - 1\}(3\rho^2 - 3 + 8\gamma^2) K(m) \], \quad (A6)$$

$$\begin{aligned} w_B = & \frac{2}{3\gamma^2} \left[1 - (1 - \rho^2)^{1/2} \left(1 - \frac{\rho^2}{4} \right) \right] \\ & + \frac{1}{45\pi\gamma^4[1 - (\gamma + \rho)^2]^{1/2}} \\ & \times \left\{ [2\gamma^6 + (29 - 7\rho^2)\gamma^4 + (26 - 34\rho^2 + 8\rho^4)\gamma^2 + 3(1 - \rho^2)^3] K(m) \right. \\ & \quad \left. + [1 - (\rho + \gamma)^2] [2\gamma^4 + (31 - 7\rho^2)\gamma^2 - 3(1 - \rho^2)^2] E(m) \right\} \\ & - \frac{2}{3\pi\gamma^2[1 - (\gamma + \rho)^2]^{1/2}} \{[1 - n(\rho + \gamma)/2\rho] \Pi(n, m) + \text{c.c.}\}, \end{aligned} \quad (A7)$$

where c.c. denotes the complex conjugate, $n = 2\rho [\rho - i(1 - \rho^2)^{1/2}]$ and $m = -4\gamma\rho/[1 - (\gamma + \rho)^2]$. To evaluate equations (A6) and (A7), careful treatments are required at the edge $\rho = 1 - \gamma$, where the argument of the elliptic integral and coefficients of $K(m)$ and $\Pi(n, m)$ in w_B apparently diverges. Since we are concerned with the planetary systems with the small ratio $R_p \ll R_s$, it is practically useful to derive the approximate expressions. In this case, we do not have to use the complicated expressions (A6) and (A7), but expand the integrands (A2) and/or (A4), (A5) in powers of $\gamma = R_p/R_s$. Then each term in the expansion with respect to γ can be analytically integrated. The results up to the second order in γ become

$$\begin{aligned} w_A \simeq & \frac{2}{3\gamma^2} (1 - \rho^2)^{1/2} \left(1 - \frac{1}{4}\rho^2 \right) - \frac{1}{16} \frac{15\rho^4 - 28\rho^2 + 16}{(1 - \rho^2)^{3/2}} \\ & - \gamma^2 \frac{1}{128} \frac{17\rho^6 - 64\rho^4 + 104\rho^2 - 32}{(1 - \rho^2)^{7/2}} + \mathcal{O}(\gamma^4), \end{aligned} \quad (A8)$$

$$w_B \simeq -\frac{1}{4} \frac{\rho^2(1 - \rho^2/4)}{(1 - \rho^2)^{3/2}} - \gamma^2 \frac{1}{128} \frac{\rho^2(24 + \rho^4)}{(1 - \rho^2)^{7/2}} + \mathcal{O}(\gamma^4). \quad (A9)$$

Substituting these expressions into equation (A3) and collecting the terms in powers of γ , we finally obtain

$$W_1 \simeq (1 - \rho^2)^{1/2} - \gamma^2 \frac{2 - \rho^2}{8(1 - \rho^2)^{3/2}} + \mathcal{O}(\gamma^4). \quad (A10)$$

Next consider the integral W_2 , whose analytical expression is also obtained through the same procedure as mentioned above. Using equations (A1), one writes equation (42) as

$$W_2 = W_1 + w_C, \quad (A11)$$

where w_C is given by

$$w_C = \frac{\gamma}{\pi \rho \cos \theta} \int_0^1 d\sigma \int_0^{2\pi} d\varphi \sigma^2 \cos \varphi \sqrt{1 - \rho^2 \sin^2(\theta - \varphi) - \{\gamma\sigma + \rho \cos(\theta - \varphi)\}^2}. \quad (A12)$$

In the above expression, the integral over σ is analytically performed and the resultant expression for integrand is expanded in powers of γ . Further integrating it over φ , we obtain

$$w_C \simeq -\gamma^2 \frac{1}{4(1-\rho^2)^{1/2}} + \mathcal{O}(\gamma^4) \quad (\text{A13})$$

Thus, the perturbative expansion for W_2 becomes

$$W_2 \simeq (1-\rho^2)^{1/2} - \gamma^2 \frac{4-3\rho^2}{8(1-\rho^2)^{3/2}} + \mathcal{O}(\gamma^4). \quad (\text{A14})$$

In Figure 15, to check the validity of the perturbation results, the approximate expressions for the integrals W_1 and W_2 are plotted as a function of ρ . The results are then compared with those obtained from the numerical integration. As is expected, the perturbative expressions (A10) and (A14) give a quite accurate approximation as long as the ratio of planetary radius to the stellar radius is small. Note that the approximation is even better for the slightly larger value $\gamma = 0.3$, with a few percent level of the fractional error.

A.2. Integrals W_3 and W_4

As for the integrals W_3 and W_4 given by equations (46) and (47), one can partially evaluate the integrals with the knowledge of the integral region (32). The resultant forms are summarized as:

$$W_3 = \frac{\pi}{6}(1-x_0)^2(2+x_0) + \int_{x_0+\zeta-\gamma}^{x_0} d\tilde{x} g(\tilde{x}; \eta_p, \gamma) \quad (\text{A15})$$

$$W_4 = \frac{\pi}{8}(1-x_0^2)^2 + \int_{x_0+\zeta-\gamma}^{x_0} d\tilde{x} \tilde{x} g(\tilde{x}; \eta_p, \gamma) \quad (\text{A16})$$

where we defined the function $g(\tilde{x}; \eta_p, \gamma)$:

$$g(\tilde{x}; \eta_p, \gamma) \equiv (1-\tilde{x}^2) \sin^{-1} \left\{ \frac{\gamma^2 - (\tilde{x} - 1 - \eta_p)^2}{1 - \tilde{x}^2} \right\}^{1/2} + \sqrt{2(1+\eta_p)(x_0 - x) \{ \gamma^2 - (\tilde{x} - 1 - \eta_p)^2 \}} \quad (\text{A17})$$

Since the above one-dimensional integrals cannot be evaluated analytically, one may derive an approximate expression applicable to the $\gamma \ll 1$ cases. Note, however, that a naive treatment by the perturbative expansion regarding γ as a small parameter can break down at $\eta_p \simeq -\gamma$. Even in the $\eta_p > \gamma$ case, perturbative expression gives a worse approximation. For accurate evaluation of the integrals, a more dedicated treatment other than the perturbative

expansion is required. One clever approach which we adopt here is to replace the function g with:

$$g(\tilde{x}; \eta_p, \gamma) \longrightarrow g(x_c; \eta_p, \gamma) \sqrt{\frac{(a - \tilde{x})(\tilde{x} - b)}{(a - x_c)(x_c - b)}}, \quad (\text{A18})$$

where we set $a = x_0 + \zeta - \gamma$, $b = x_0$ and $x_c = (a + b)/2$. And we use the following integral formula:

$$\int_a^b dx \sqrt{\frac{(a - x)(x - b)}{(a - x_c)(x_c - b)}} = \frac{\pi}{4}(b - a). \quad (\text{A19})$$

Then, one can approximate the one-dimensional integrals in equations (A15) and (A16) as follows:

$$\int_{x_0 + \zeta - \gamma}^{x_0} d\tilde{x} g(\tilde{x}; \eta_p, \gamma) \longrightarrow \frac{\pi}{4} (\gamma - \zeta) g(x_c; \eta_p, \gamma), \quad (\text{A20})$$

$$\int_{x_0 + \zeta - \gamma}^{x_0} d\tilde{x} \tilde{x} g(\tilde{x}; \eta_p, \gamma) \longrightarrow \frac{\pi}{8} (\gamma - \zeta)(2x_0 + \zeta - \gamma) g(x_c; \eta_p, \gamma). \quad (\text{A21})$$

As long as the planetary transit system with $\gamma \ll 1$, the above expression in fact gives an accurate prescription. Note, however, that a naive use of the formulae (A20) and (A21) leads to the inconsistent radial velocity curves, which do not satisfy the junction condition at $\eta_p = -\gamma$:

$$W_3 = \pi \gamma^2 W_1|_{\rho=1-\gamma}, \quad W_4 = \pi \gamma^2 (1 - \gamma) W_2|_{\rho=1-\gamma}. \quad (\text{A22})$$

To keep the consistency, we devise to modify equations (A20) and (A21) so as to satisfy the junction condition (A22) by multiplying the numerical factor. The final expressions for W_3 and W_4 become:

$$W_3 \simeq \frac{\pi}{6} (1 - x_0)^2 (2 + x_0) + \frac{\pi}{2} \gamma (\gamma - \zeta) \frac{g(x_c; \eta_p, \gamma)}{g(1 - \gamma; -\gamma, \gamma)} W_1(1 - \gamma), \quad (\text{A23})$$

$$W_4 \simeq \frac{\pi}{8} (1 - x_0)^2 (1 + x_0)^2 + \frac{\pi}{2} \gamma (\gamma - \zeta) x_c \frac{g(x_c; \eta_p, \gamma)}{g(1 - \gamma; -\gamma, \gamma)} W_2(1 - \gamma). \quad (\text{A24})$$

In figure 16, substituting equations (A10) and (A14) into the above results, the approximate expressions for W_3 and W_4 are depicted as a function of η_p . Albeit the tricky treatment, it turns out that the expressions (A23) and (A24) give an accurate approximation for the range of our interest. Compared to the integrals W_1 and W_2 , the fractional error of the approximations seems slightly large, however, the contribution of the integrals W_3 and W_4 to the radial velocity shift Δv_s is relatively small. With a typical parameter $\gamma \sim 0.1$, the resultant fractional error remains only a few per cent level.

REFERENCES

Alonso, R., Bron, T.M., Torres, G., Latham, D.W. Sozzetti, Al., Mandushev, G., Belmonte, J.A., Charbonneau, D., Deeg, H.J., Dunham, E.W., O'Donovan, F.T., and Stefanik, R.P. 2004, ApJ, 613, L153

Bouchy, F., Pont, F., Santos, N.C., Melo, C., Mayor, M., Queloz, D., and Udry, S. 2004, A&A, 421, L13

Brown, T.M. et al., 2001, ApJ, 552, 699.

Butler, R.P., Marcy, G.W., Williams, E., McCarthy, C., Dosanjh, P., & Vogt, S.S. 1996, PASP, 108, 500

Charbonneau, D., Saurabh, J., & Robert, N.W. 1998, ApJ507, L153.

Charbonneau, D. et al., 1999, ApJ522, L145.

Charbonneau, D. et al., 2000, ApJ529, L45.

Charbonneau, D. et al. 2002, ApJ, 568, 377.

Claret, A. 2000, A&A, 363, 1081

Coustenis, A., et al. 1998, in ASP Conf.Ser., 134, 296.

Désert, J.-M., et al. 2003, to be published in the proceedings of the XIXth IAP Colloquium “Extrasolar Planets, Today And Tomorrow” (astro-ph/0312383)

Gizon, L., & Solanki, S. K. 2003, ApJ, 589, 1009.

Henry, G.W. et al., 2000, ApJ, 529, L41.

Hosokawa, Y. 1953, PASJ, 5, 88.

Konacki, M., Torres, G., Jha, S. and Sasselov, D. D., 2003, Nature, 421, 507.

Kopal, Z. 1999, *Mathematical Theory of Stellar Eclipses* (Kluwer, Dordrecht).

Lecavelier des Etangs, A. et al. 2004, A&A, submitted.

Liang, M., Parkinson, C.D., Lee, A.Y.-T., Yung, Y.L., & Seager, S. 2003, ApJ, 596, L247.

Lin, D.N.C., Bodenheimer, P., Richardson, D.C. 1996, Nature, 380, 606

McLaughlin, D. B. 1924, ApJ, 60, 22

Marcy, G.W. & Butler, R.P. 1996, ApJ, 464, L147.

Mayor, M. and Queloz,D., 1995, Nature, 378, 355.

Mazeh, T., Naef, D., Torres, G.,et al. 2000, ApJ, 532, L55.

Moutou, C., Coustenis, A., Schneider, J., St Gilles, R., Mayor, M., Queloz, D., & Kaufer, A. 2001, A&A, 371, 260.

Moutou, C., Coustenis, A., Schneider, J., Queloz, D., & Mayor, M., 2003, A&A, 405, 341.

Murray, C.D. and Dermott, S.F., 1999, *Solar System Dynamics* (University of Cambridge Press: Cambridge)

Naef,D., Mayor, M., Beuzit, J.L., Perrier, C., Queloz, D., Sivan, J.P., & Udry, S. 2004, A&A, 414, 351.

Noguchi, K., et al. 1999, PASJ, 54, 855.

Noyes, R.W., Hartmann, L.W., Baliunas, S.L., Duncan, D.K., and Vaughan, A.H. 1985, ApJ, 279, 763.

Pollack, J.B., Hubickyj, O., Bodenheimer, P., et al. 1996, Icarus, 124, 62

Queloz, D., Eggenberger, A., Mayor, M., Perrier, C., Beuzit, J.L., Naef, D., Sivan, J.P., and Udry, S., 2000, A&A, 359, L13.

Rossiter, R. A. 1924, ApJ69, 15.

Rasio, F. A., Tout, C. A., Lubow, S. H., and Livio, M. 1996, ApJ, 470, 1187.

Santos, N.C., Bouchy, F., Mayor, M., et al. 2004, A&A, in press (astro-ph/0408471)

Sato, B., Kambe, E., Takeda, Y., Izumiura, H., & Ando, H. 2002, PASJ, 54, 873.

Snellen, I. A. G. 2004, MNRAS, submitted (astro-ph/0403101)

Valenti, J.A., Butler, R.P., & Marcy, G.W. 1995, PASP, 107, 966

Vidal-Madjar, A., Lecavelier des Etangs, A., Désert, J.-M., Ballester, G.E., Ferlet, R., Hébrard, G., & Mayor, M. 2003, Nature, 422, 143.

Winn, J.N., Suto, Y., Turner, E.L., Narita, N., Frye, B.L., Aoki, W., Sato, B., & Yamada, T. 2004, PASJ, 56, 655

Wittenmyer, R. et al. 2003, to be published in the proceedings of the XIXth IAP Colloquium
“Extrasolar Planets, Today And Tomorrow”

Table 1. List of notations

Variables	Definition	Meaning
m_p	Sec.2	planet mass
m_s	Sec.2	stellar mass
a	Fig.1	semi-major axis
e	Fig.1	eccentricity of planetary orbit
ϖ	Fig.1	minus of the longitude of the line-of-sight
i	Fig.2	inclination between normal direction of orbital plane and y -axis
r_p	Eq.[1]	distance between star and planet (see Fig.1)
f	Eq.[2]	true anomaly (see Fig.1)
E	Eq.[2]	eccentric anomaly
n	Eq.[3]	mean motion
M	Eq.[4]	mean anomaly
I_s	Fig.2	inclination between stellar spin axis and y -axis
λ	Fig.3	angle between z -axis and normal vector \hat{n}_p on (x, z) -plane
Ω_s	Eq.[12]	angular velocity of star (see Fig.2)
R_s	Sec.4	stellar radius
R_p	Sec.4	planet radius
ϵ	Eq.[38]	limb darkening parameter
V	Sec.6	stellar surface velocity, $R_s\Omega_s$
\mathbf{X}_p	Sec.4	position of the planet
γ	Eq.[25] below	ratio of planet radius to stellar radius, R_p/R_s
η_p	Eq.[28]	see Fig.6
x_0	Eq.[33]	see Fig.6
z_0	Eq.[33]	see Fig.6
ζ	Eq.[34]	see Fig.6

Table 2. Parameters of the HD209458 system

Parameters	Estimated values	Fractional errors
m_s	$1.1 \pm 0.1^\dagger$ [M_\odot]	9.1%
m_p	$0.69 \pm 0.05^\dagger$ [M_J]	7.2%
e	$0^\S - 0.1^\ddagger$	
a	$0.0468^\dagger \pm 0.0014^\P$ [AU]	3.0%
ϖ	$100^\circ \ddagger$	
P_{orb}	$3.52474 \pm 0.00007^\dagger$ [day]	0.002%
R_s	$1.146 \pm 0.050^\dagger$ [R_\odot]	4.4%
R_p	$1.347 \pm 0.060^\dagger$ [R_J]	4.5%
i	$86^\circ.1 \pm 0^\circ.1^\S$	0.1%
ϵ	$0.64 \pm 0.03^\dagger$	4.7%

\P This error is calculated from those of m_s , m_p , and P_{orb} .

\dagger Brown et al.(2001)

\ddagger <http://exoplanets.org/esp/hd209458/hd209458.html>

\S <http://www.obspm.fr/encycl/HD209458.html>

Table 3. Spin parameters derived by Queloz et al. (2000) and notational differences

This paper	Queloz et al. (2000)	Best-fit solutions †
$V \sin I_s$	$v \sin i$	3.75 ± 1.25 [km s^{-1}]
$\text{sgn}(\lambda) \cos^{-1}\{\cos \lambda \sin i\}$	α	$\pm 3.9^\circ_{-21^\circ}^{+18^\circ}$
λ	$\text{sgn}(\alpha) \cos^{-1} \left\{ \frac{\cos \alpha}{\sqrt{1 - \cos^2 \Omega_p \sin^2 \alpha}} \right\}$	0 $^\circ$ for $(\alpha, \Omega_p) = (3.9^\circ, 0^\circ)$ 21.7 $^\circ$ for $(\alpha, \Omega_p) = (22^\circ, 100^\circ)$ -24.7 $^\circ$ for $(\alpha, \Omega_p) = (-25^\circ, 80^\circ)$

† The parameter Ω_p is related to the inclination angle and is constrained through $\cos \Omega_p = -\cos(86.1^\circ) / \cos \alpha$.

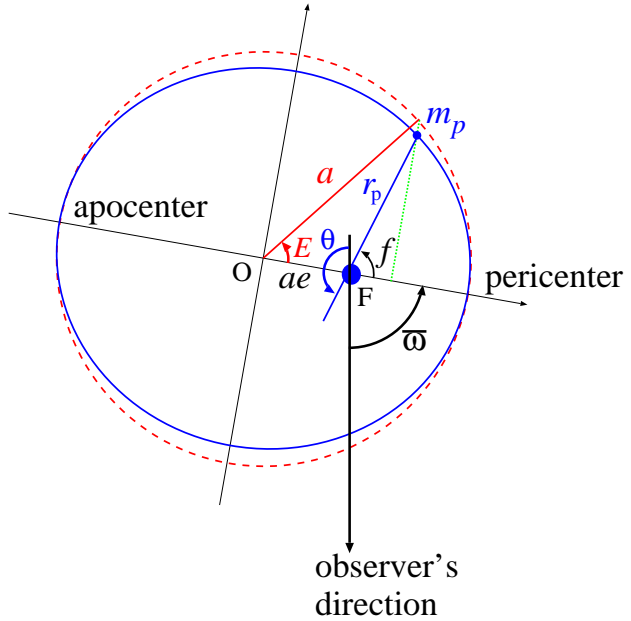


Fig. 1.— A schematic top view of the planetary orbit. The star is located at the focus point F (see Table 1 for meaning of symbols).

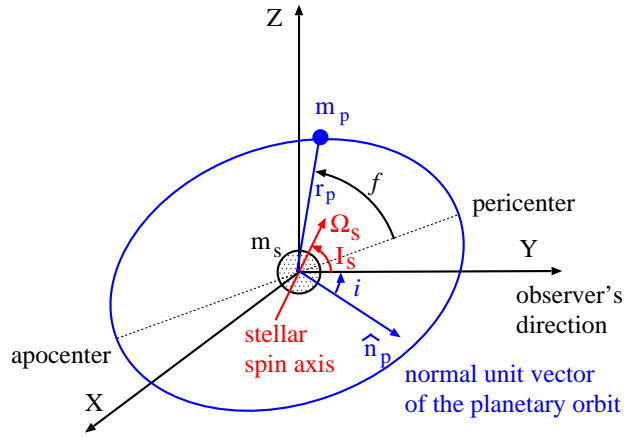


Fig. 2.— A schematic configuration of the stellar spin axis, the planetary orbital plane and the observer's line-of-sight (see Table 1 for meaning of symbols).

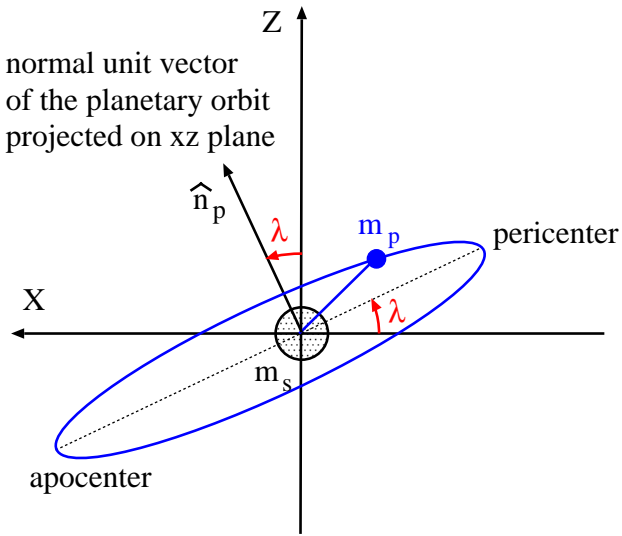


Fig. 3.— A projected view of the planetary orbital plane from the line-of-sight (Y-axis in this case).

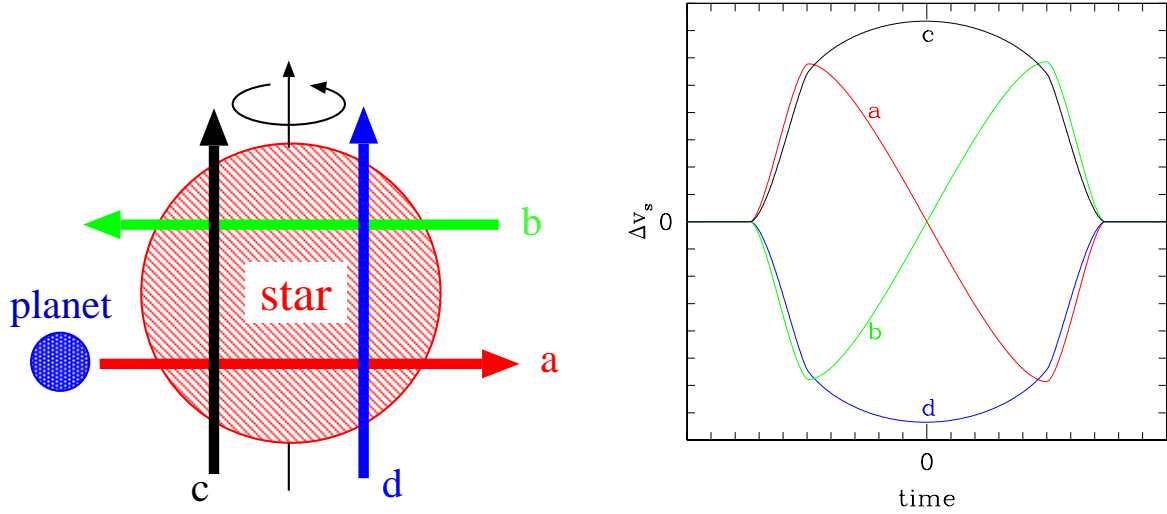


Fig. 4.— A schematic illustration of the velocity curve anomaly due to the RM effect. The four different paths of a planet, $a \sim d$, in the left panel correspond to the velocity curves in the right panel.

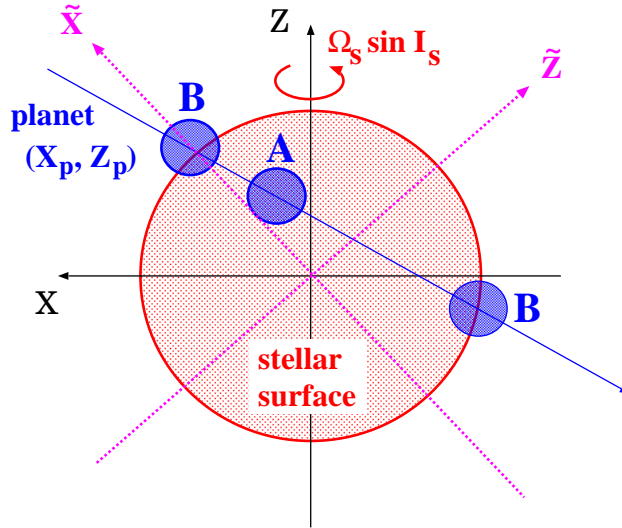


Fig. 5.— The planetary transit; ingress, complete transit, and egress phases.

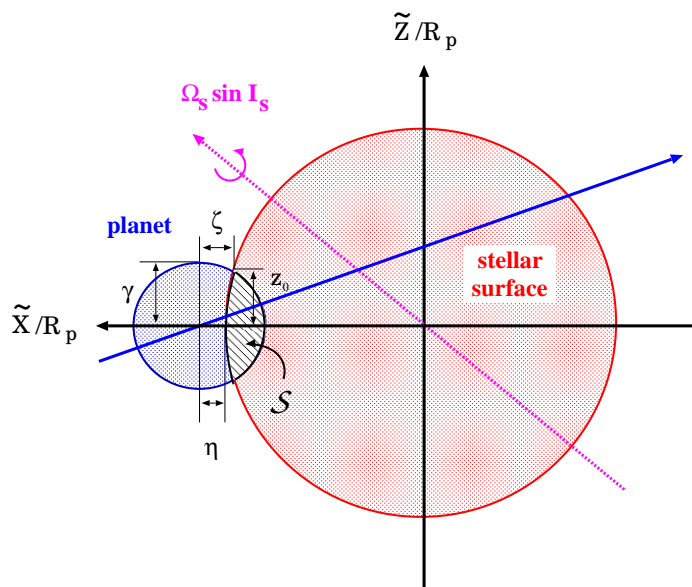


Fig. 6.— A schematic illustration of the configuration of the system at ingress of the planet in the new coordinate.

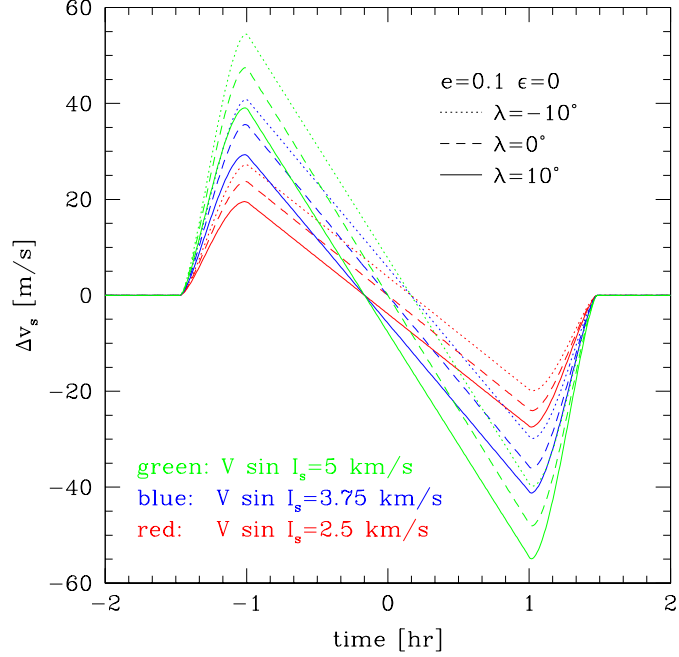


Fig. 7.— Analytic radial velocity curves for the RM effect without stellar limb darkening ($\epsilon = 0$).

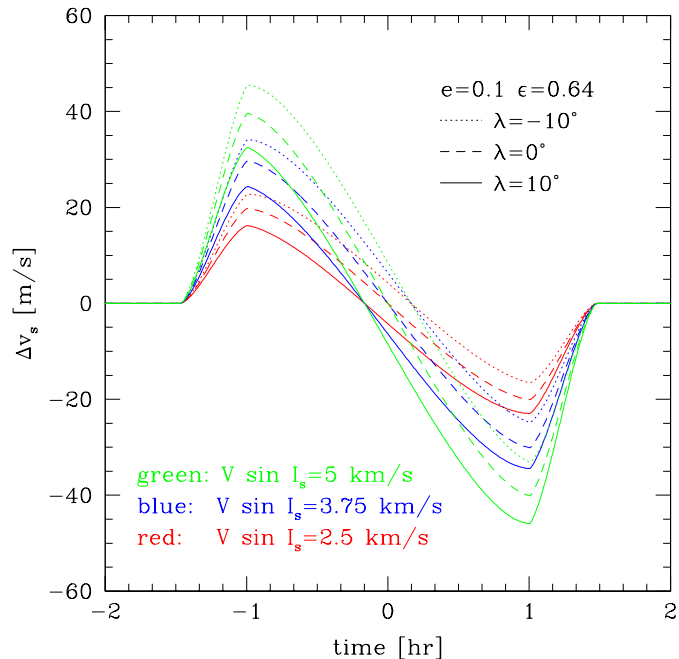


Fig. 8.— Same as Fig.7 with with linear limb darkening effect ($\epsilon = 0.64$).

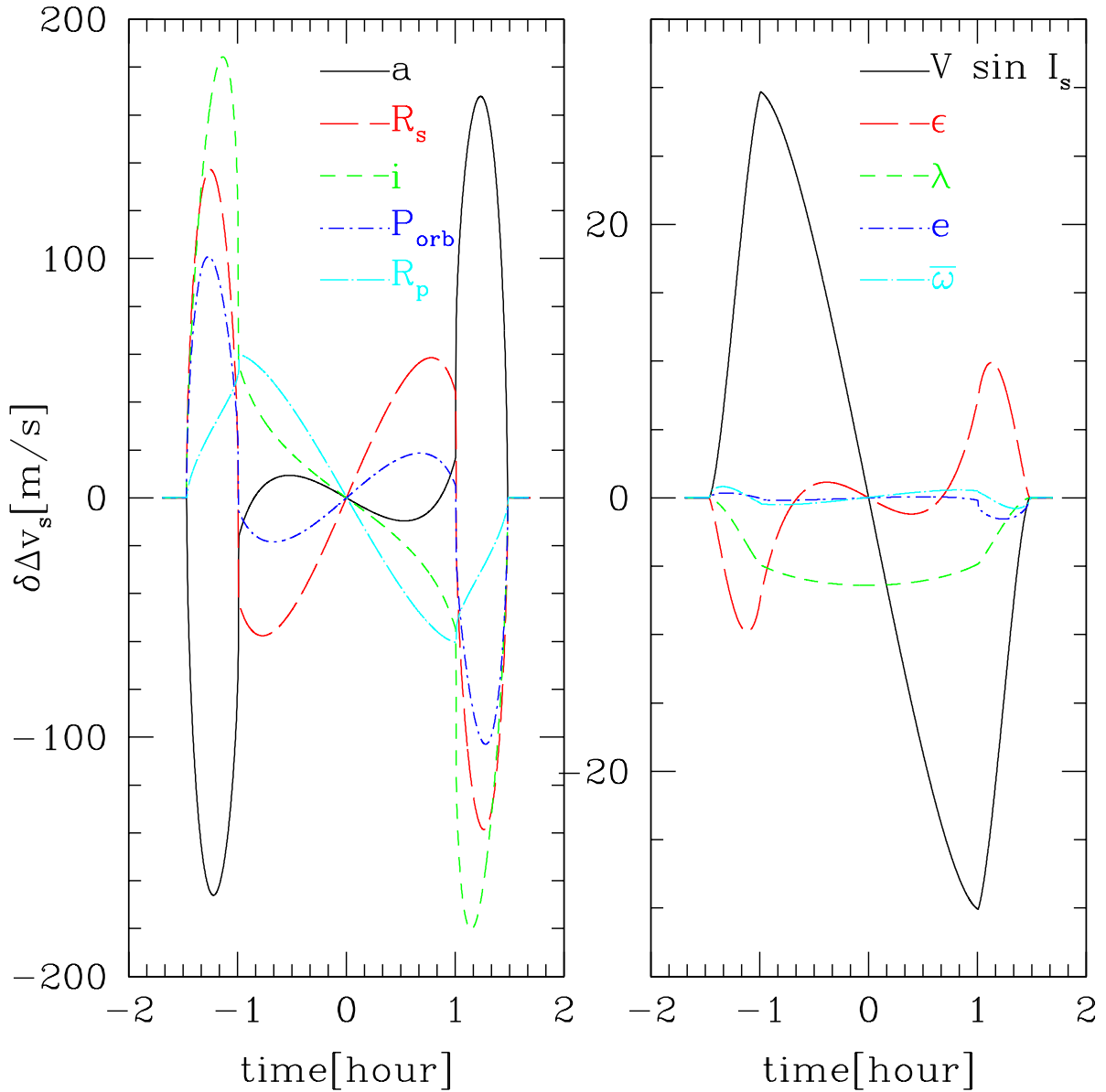


Fig. 9.— The variation of radial velocity shift with respect to a parameter variation $p \rightarrow p + dp$ as a function of time. The vertical axis denotes the variation of radial velocity shift normalized by the fractional error in each parameter dp/p (eqs. [52] and [53] for *Left* and *Right* panels, respectively). These quantities are evaluated around the fiducial values for the HD209458 system summarized in Table 2 using the analytic formulae for the RM effect.

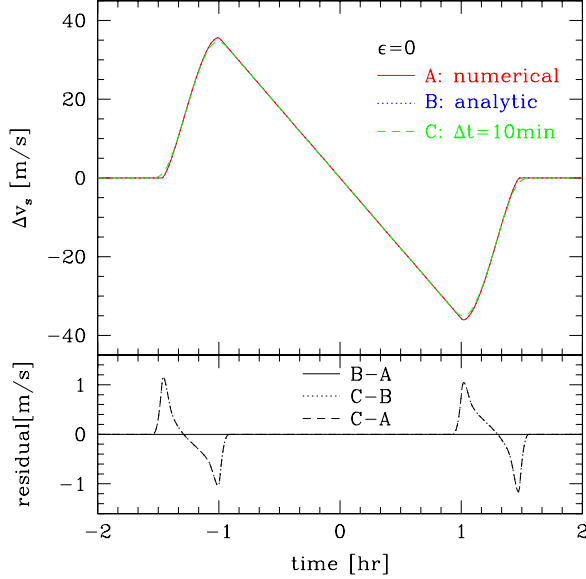


Fig. 10.— Comparison of different models of the radial velocity anomaly curves for the HD209458 system without the limb darkening ($\epsilon = 0$). The Upper panel shows the radial velocity shifts obtained from the numerical evaluation of the expression (20) (*solid*), the analytic formulae with and without the effect of exposure time (*dotted* and *dashed*). The lower panel shows the residuals between the two radial velocity shifts among three curves.

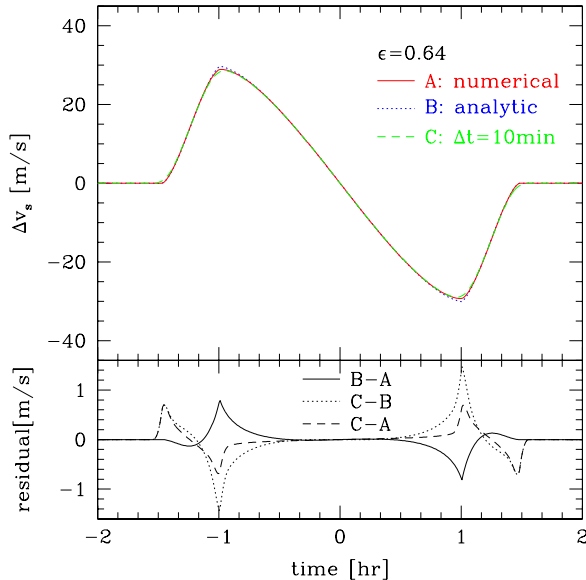


Fig. 11.— Same as Fig.10, but with limb darkening ($\epsilon = 0.64$).

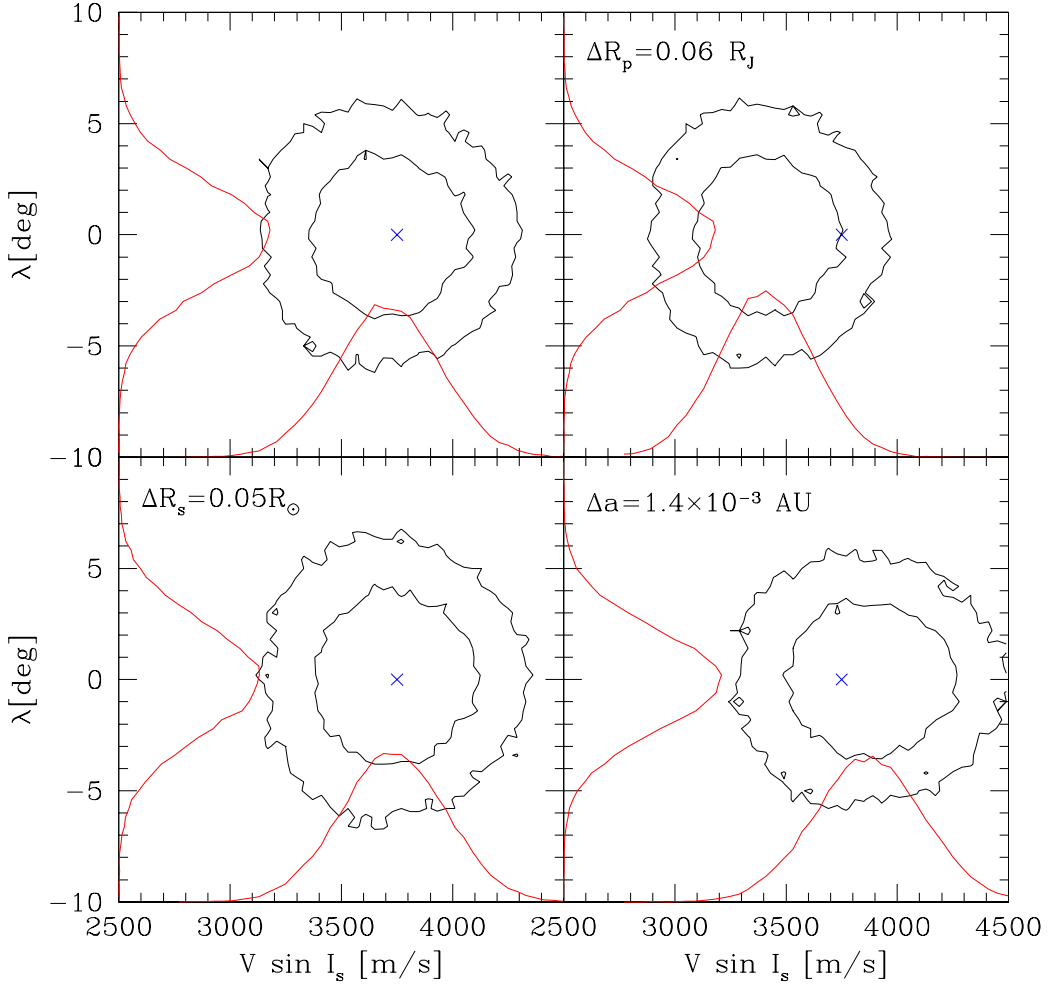


Fig. 12.— Joint probability distribution of the best-fit parameters ($V \sin I_s$, λ) in the likelihood analysis for the mock HD209458 observation. We adopt the prior assumption for fiducial parameters (*upper-left*), $R_s = 1.407[R_J]$ (*upper-right*), $R_s = 1.196[R_\odot]$ (*lower-left*) and $a = 0.0482[\text{AU}]$ (*lower-right*). In each panel, the cross indicates the correct values of ($V \sin I_s$, λ) and the contour levels around it represent the 1, 2- σ levels of the probability distribution. The solid lines projected onto the horizontal (vertical) axis represent the probability distribution of $V \sin I_s$ (λ). Note that all the mock data created in the likelihood analysis assume the parameters listed in Table 2. Thus, except for the upper-left panel, the difference between incorrect prior assumption and correct value for (R_p, R_s, a) was used in each panel.

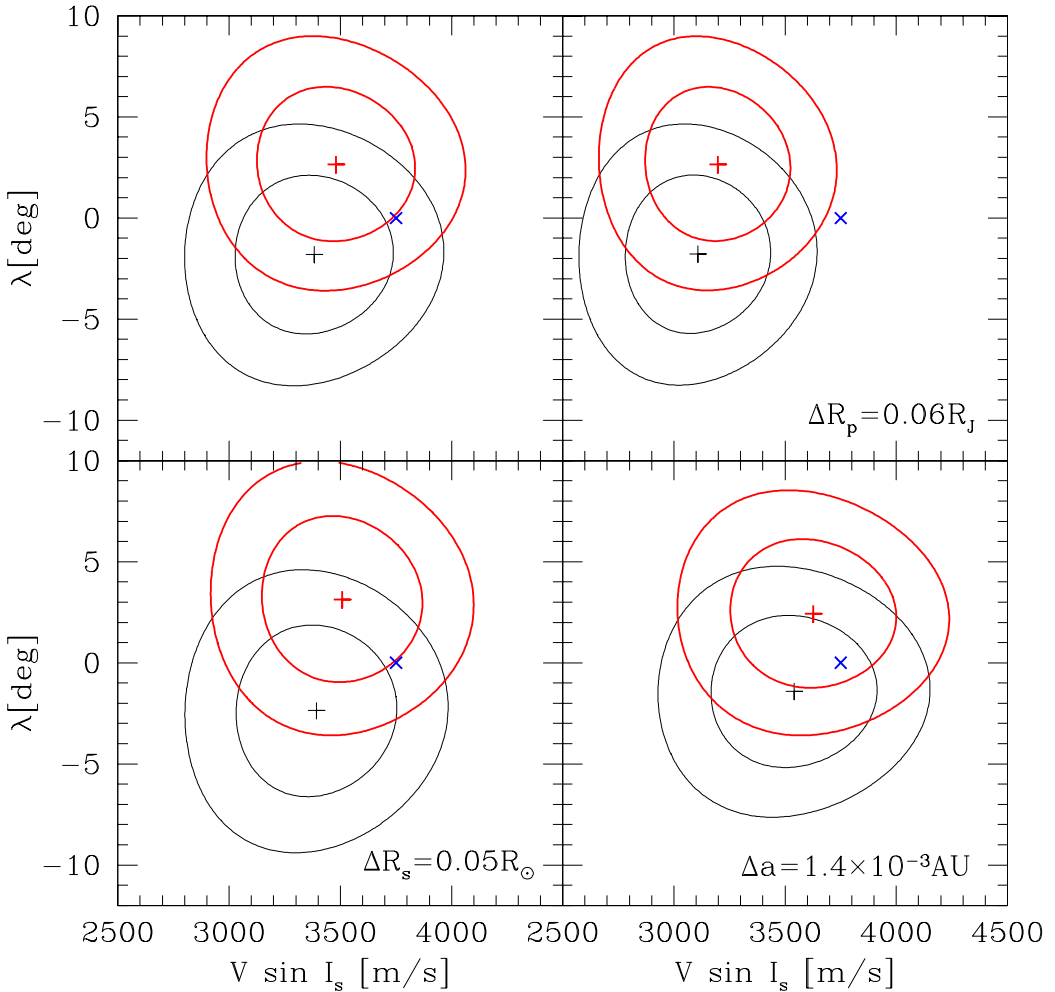


Fig. 13.— Expected constraints on the spin parameters ($V \sin I_s$, λ) from the χ^2 fit to the mock data of radial velocity curves for the HD209458 system. The thin and the thick lines show the results obtained from the different mock samples created according to the same parameters as listed in table 2. The two contour curves in each line width represent the 1 and 2σ confidence levels. The location of the symbols \times represents the true value of the spin parameters ($V \sin I_s$, λ), while the location of the symbols $+$ indicates the best-fit parameters, which were estimated under the prior assumption for the limb darkening coefficient and the orbital eccentricity as right parameters (*upper-left*), $\Delta R_p = 0.06 R_J$ (*upper-right*), $\Delta R_s = 0.05 R_\odot$ (*lower-left*) and $\Delta a = 1.4 \times 10^{-3}$ [AU] (*lower-right*).

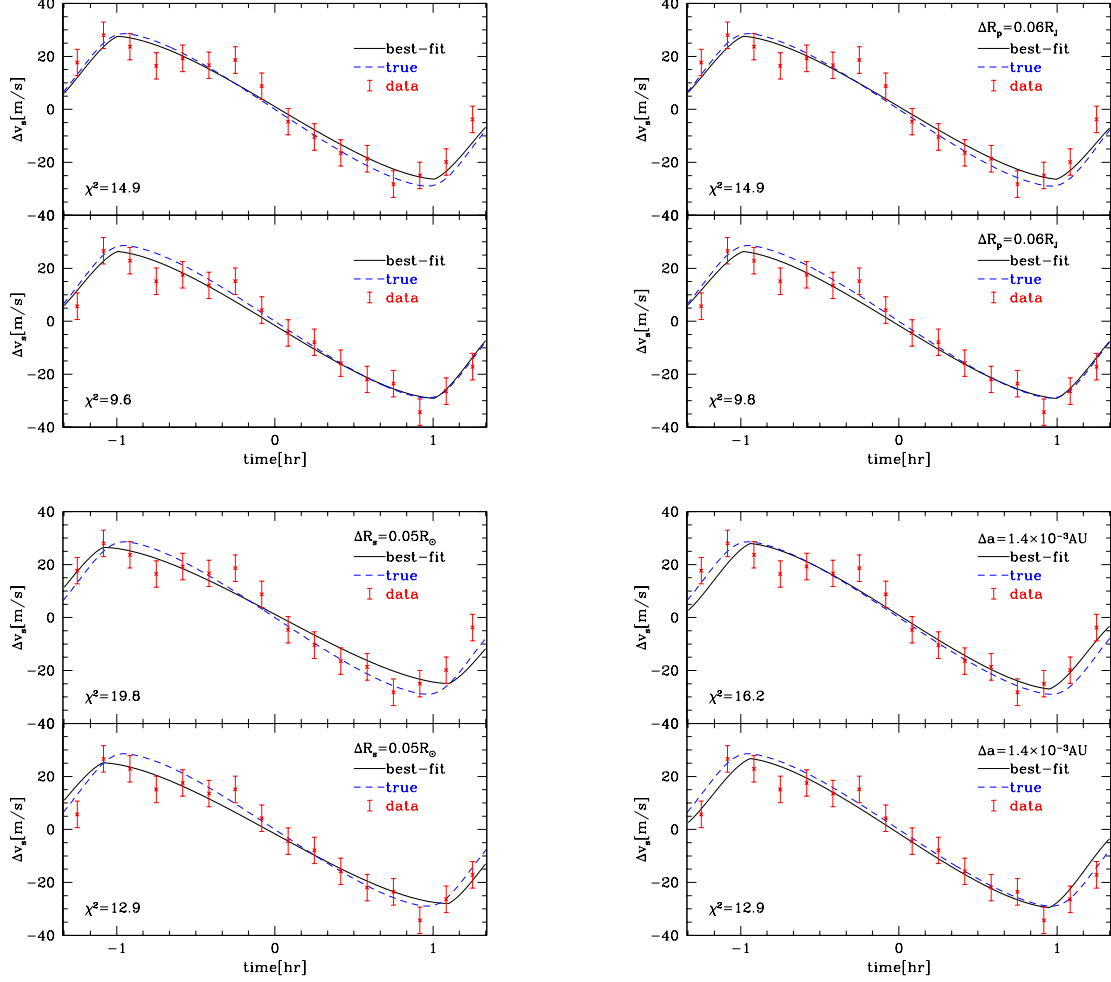


Fig. 14.— Comparison between the mock data for the radial velocity curves used in Fig.13 and the best-fit curves for the parameters ($V \sin I_s$, λ) (*solid*) determined under the prior assumption of (ϵ , e): fiducial parameters (*upper-left*); $\Delta R_p = 0.06[R_J]$ (*upper-right*); $\Delta R_s = R_\odot$ (*lower-left*); $\delta a = 1.4 \times 10^{-3}$ AU (*lower-right*). The result depicted in the upper(lower) window of each panel show the one corresponding to the thin(thick) contour lines in Fig.13. For comparison, we also plot the correct radial velocity curves in each plot (*dashed*).

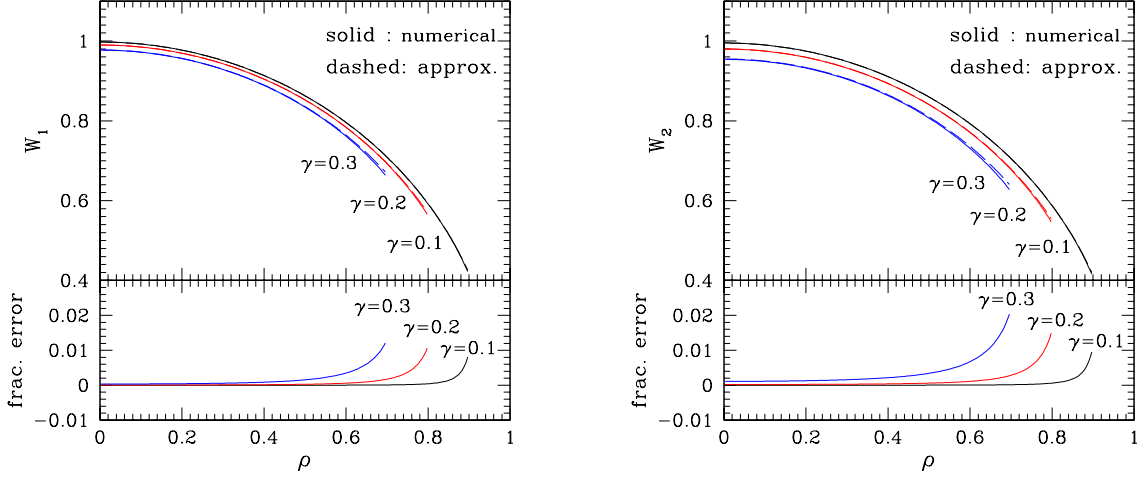


Fig. 15.— *Upper:* approximate vs numerical evaluations of the integrals W_1 (*left*) and W_2 (*right*) as a function of $\rho = \sqrt{X_p^2 + Z_p^2}/R_s$. The solid lines represent the numerical evaluation of equations (A3) and (A11), while the dashed lines are the approximation based on the perturbative expansions (A10) and (A14). Note that the variable ρ runs from 0 to $1-\gamma$. *Lower:* fractional errors $W^{(\text{approx})}/W^{(\text{num})} - 1$ for the integrals W_1 (*left*) and W_2 (*right*).

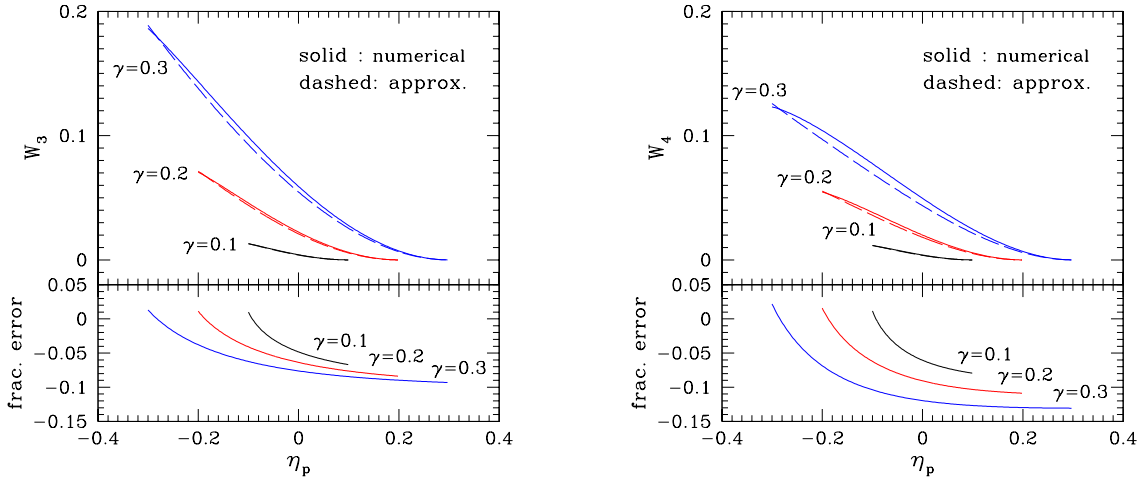


Fig. 16.— *Upper:* approximate vs numerical evaluations of the integrals W_3 (*left*) and W_4 (*right*) as a function of η_p . The solid lines represent the numerical evaluation of equations (A15) and (A16), while the dashed lines are the approximation based on the perturbative expansions (A23) and (A24). Note that the variable η_p runs from $-\gamma$ to γ . *Lower:* fractional errors $W^{(\text{approx})}/W^{(\text{num})} - 1$ for the integrals W_3 (*left*) and W_4 (*right*).